PCCP

PAPER

View Article Online
View Journal | View Issue

Cite this: *Phys. Chem. Chem. Phys.*, 2015, **17**, 23503

The nature of photogenerated charge separation among different crystal facets of $BiVO_4$ studied by density functional theory

Taifeng Liu,†[ab] Xin Zhou,†[a] Michel Dupuis[c] and Can Li*[a]

Received 22nd July 2015,
Accepted 6th August 2015

DOI: 10.1039/c5cp04299b

www.rsc.org/pccp

Charge separation among different crystal facets of a semiconductor has been observed experimentally, but the underlying reasons behind this phenomenon are unknown. In this work, the activation energies of carrier hopping and the mobility of electron/hole transport along seven low-index crystal orientations of bulk $BiVO_4$ have been calculated using a small polaron model. The calculated mobility and our previous experimental results reveal that there is a parallel relationship between the carrier mobility along the crystal axis and the carrier preferred accumulation on the corresponding crystal facets. It is proposed that the mobility of electrons (or holes) along the crystal axis [*hkl*] might be essentially related to the charge separation among the indices of corresponding facets (*hkl*); namely, the mobility of electrons (or holes) along the crystal axis [*hkl*] is the largest among all possible crystal axes, and the photogenerated electrons (or holes) tend to be accumulated on the indices of the corresponding facet (*hkl*) when the surface factors like surface band bending, surface energetic differences, *etc.* are not considered.

1. Introduction

Solar driven water splitting with semiconductor-based photocatalysts is one of the most ideal routes to convert solar energy into chemical fuel.[1–3] However, most semiconductor-based photocatalysts provide a quite low overall energy conversion efficiency that is far from practical applications. One of the key issues related to this problem is the limited charge separation efficiency upon photo-excitation, which largely depends on the intrinsic electronic and structural properties of semiconductors.[4,5] To improve the photocatalytic activity, various strategies have been used to promote charge separation in semiconductor-based photocatalysts.[6] For example, proper junctions formed between two kinds of semiconductors, or two phases of the same semiconductor, could lead to enhanced activity in hydrogen and/or oxygen evolution reaction.[7,8]

Recent investigations[9–11] demonstrated that crystal facet engineering of semiconductors has become an important strategy employed to promote the separation of photoexcited electrons and holes. For instance, efficient charge separation can be achieved on different crystal facets of $BiVO_4$, evidenced by the observed phenomenon that the reduction and oxidation reactions take place separately on the (010) and (110) facets under photo-irradiation.[9] Recent reports showed that for single crystals of anatase TiO_2, the noble metals (Au, Ag, and Pt) were selectively photodeposited on the exposed (010) facet, and metal oxides (PbO_2 and MnO_x) were selectively photodeposited on the exposed (110) facet. These results suggest that photogenerated electrons and holes are mainly accumulated on the (010) and (110) facets, respectively.[10] Wang and co-workers reported that BiOCl@Au/MnO_x hierarchical structures obtained by selectively depositing Au and MnO_x on the (001) and (110) crystal facets of BiOCl result in a significant enhancement of photocatalytic activity in a water splitting reaction.[11] Several reasons for the selective photodeposition have been proposed. According to the theory advocated by Ohno *et al.*, photoillumination on a semiconductor could result in the preferred migration of holes and electrons to specific crystal facets.[12] Miseki *et al.* ascribed the structure-directed deposition of Au, Ni, and PbO_2 on $BaLaTiO_4$ to preferred sorption phenomena.[13] Wang *et al.* suggested that the different energy levels of the conduction band and valance bands for different facets and the internal electronic field along a particular axis in a crystal are possible reasons for these experimental observations.[11] However, the nature of photogenerated charge separation among different facets of a single crystal of semiconductor remains unclear.

When semiconductors are excited by photons with energy equal to or higher than their energy band gaps, electrons are

[a] *State Key Laboratory of Catalysis, Dalian Institute of Chemical Physics, Chinese Academy of Sciences, Dalian National Laboratory for Clean Energy, 457 Zhongshan Road, Dalian 116023, P. R. China. E-mail: canli@dicp.ac.cn*
[b] *Graduate University of Chinese Academy of Sciences, Beijing 100049, P. R. China*
[c] *Department of Chemical and Biological Engineering and Computation and Data-enabled Science and Engineering Program University at Buffalo, State University of New York Buffalo, NY 14260, USA*
† These authors contributed equally to this work.

excited from the valence band (VB) to the conduction band (CB). The photo-generated electrons and holes could recombine in bulk or on the surface of the semiconductor within a very short time, releasing energy in the form of heat or photons. The surviving photogenerated electrons and holes, without recombination, migrate to the surface of the semiconductor and participate in reduction and oxidation reactions, respectively. Commonly the semiconductor possesses anisotropic properties, so the transport of the charge carrier will be diverse along the different crystal orientations.

In this work, we presumed that the intrinsic electron and hole transport properties of anisotropic semiconductors might essentially be associated with charge separation between different facets. We used monoclinic scheelite (ms-)$BiVO_4$ as a model to investigate charge separation among different facets. We investigated the transport of the charge carrier in the bulk material by the DFT+U approach combined with Marcus/Holstein theory.[14,15] Our calculations show that (1) the mobility of electrons is predicted to be much larger than that of holes in the same crystal orientation; (2) surprisingly, we found that in the exposed facets of the crystal, the mobility of electrons (or holes) along the crystal axis [*hkl*] is the largest, and the photogenerated electrons (or holes) tend to be accumulated on the indices of the corresponding facet (*hkl*). ([*hkl*] is the indices of the crystal direction and (*hkl*) is the indices of the corresponding crystal plane)

2. Computational methods and details

Theoretical calculations based on density functional theory (DFT) have been proven to be very useful and powerful for elucidating the structural, electronic, physical and chemical properties of semiconductor materials.[16–18] To understand the intrinsic mechanism concerning photoexcited electron and hole transport through the crystal, a small polaron model has been used to investigate metal-oxide semiconductors[19,20] and proven to be valid both experimentally and theoretically.[21,22] A polaron commonly results from charge localization accompanied by lattice distortions: a small polaron localized at the atomic scale,[23,24] and a large polaron spreads over many lattice sites. As for $BiVO_4$, it was demonstrated that a small polaron hopping conduction mechanism dominates at temperatures from 250 to 400 K.[25,26] In this work, we studied the transport of electrons and holes in $BiVO_4$ at room temperatures using a small polaron model.

We performed spin-polarized DFT calculations using the Vienna *ab initio* Simulation Package (VASP).[27,28] The exchange correlation potential was described by the Perdew–Burke–Ernzerhof (PBE) functional within the generalized gradient approximation.[29] The projector-augmented wave method was applied to describing electron–ion interactions.[30,31] We used a $2 \times 2 \times 2$ supercell with 192 atoms as our model and a $2 \times 1 \times 2$ K-point mesh was used to calculate electronic structures. The structures were relaxed until all forces on atoms were less than 0.01 eV $Å^{-1}$, and a plane-wave cutoff energy of 400 eV was employed.

To overcome the self-interaction error of standard DFT methods, we employed a DFT+U approach to study the polaron structures involved in adding an extra electron to, or removing an electron from, bulk supercells.[32] Within this framework, the on-site Coulomb interaction U and exchange parameter J are the determining factors for the magnitude of the correction. Here, we used a fixed J value of 1.0 eV and varied the U value to find an appropriate parameter $U_{eff} = U-J$ for both electron and hole localization in $BiVO_4$. Previous calculations and experimental results found that the valence band maximum (VBM) of bulk $BiVO_4$ mainly consists of O 2p orbitals, and the conduction band minimum (CBM) is primarily composed of V 3d orbitals.[33–35] We attempted to localize the electron or hole by varying the U_{eff} values from 1.0 to 11.0 eV for both O 2p and V 3d orbitals. We made our efforts to find an optimal U_{eff} in Section 3.

Small polaron mobility in metal-oxide solids is typically modeled within the framework of Marcus/Holstein theory, with the parameters derived from DFT calculations.[19,20] Within the framework of Marcus/Holstein theory, a basic polaron transfer process involves three relevant states: the initial, final, and transition states. In the initial state, the polaron is localized on one particular atom (such as O) site. When the polaron moves to an adjacent site (another O atom with the same coordinative environment), the final state is formed. In a period crystal, the initial and final states are identical. With the electron and hole localized on equivalent initial and final sites, we can use a linear interpolation scheme to calculate the polaron transfer pathway. $\mathbf{R_1}$ and $\mathbf{R_2}$ are defined as vectors of the three-dimensional coordinates of all atoms in the initial and final polaron states, respectively. Then, the coordinates of all atoms along the hopping path can be approximated as $\mathbf{R}_x = x\mathbf{R_1} + (1-x)\mathbf{R_2}$, where x varies in the range from 0.0 to 1.0. Where $x = 0.5$ corresponds to the midpoint that happens to be the transition state due to the translation or symmetry equivalence of the final and initial states. The energy barrier ΔG is calculated as $\Delta G = E_{R_{0.5}} - E_{R_1}$. Using Einstein's formula, the electron/hole mobility can be estimated approximately by

$$\mu = \frac{eD}{k_B T} = \frac{e(1-c)a^2\nu_0 \exp\left(-\frac{\Delta G}{k_B T}\right)}{k_B T} \quad (1)$$

where $(1-c)$ is the probability that a neighboring site is available for hopping, ΔG is the energy barrier, ν_0 is the longitudinal optical phonon frequency, k_B is Boltzmann's constant, T is the temperature, and a is the transfer distance. In this calculation, $(1-c) \approx 1$, $T = 300$ K, and $\nu_0 = 10^{13}$ Hz.[36] All low-index crystal orientations of [100], [010], [001], [110], [101], [011], and [111] were selected as possible polaron transfer pathways.

3. Results and discussion

Determination of an appropriate U_{eff} parameter is necessary for DFT+U calculations in order to correct the electron self-interaction in DFT. There is no universal U value that works equally well for all materials or for all properties of interest. We selected the U_{eff} value as follows. Firstly, we chose to examine

how the band gap was affected by the choice of U_{eff} values. The band gap *versus* the U_{eff} values is shown in Fig. 1. Experimentally, the band gap has been found to be 2.4 eV for $BiVO_4$. From Fig. 1, we found that although the U_{eff} value reaches 12 eV, the band gap is still far away from the experimental value. The change in the band gap with the increase of the U_{eff} value is within 0.1 eV. So for $BiVO_4$, it is hard to find a suitable U_{eff} which results in the band gap in satisfactory accord with the experiment. But we can find something useful to determine the U_{eff} values shown in Fig. 1. There are three convergent trend sections in it. The first section is the U_{eff} value from 3 eV to 5 eV, the second section is the U_{eff} value from 6 eV to 8 eV, and the third section is the U_{eff} value from 9 eV to 12 eV. The band gap does not change when U_{eff} = 4 and 5 eV in the first section and the band gap is almost the same when U_{eff} = 6, 7, and 8 eV in the second section. When increasing the U_{eff} value, the band gap has no a little bit of change. This is probably because these U_{eff} values will not reflect the properties of this material. In the third section, the band gap increases slowly to a convergent value from U_{eff} = 9 eV. These U_{eff} values could reflect the properties of this material correctly and we decided preliminarily that the U_{eff} value should begin from 9 eV.

Secondly, we attempted to localize the electron or hole by varying the U_{eff} values from 1 to 11 eV. We found that when U_{eff} is less than 5 eV, the electron is delocalized. When the U_{eff} value is less than 6 eV, the hole is delocalized. Similar phenomena were also observed for bulk TiO_2 cases.[19] As shown in Fig. 2 and 3, we gave the position of the trap state in the band gap by varying U_{eff} values for the electron from 5 to 11 eV and for the hole from 6 to 11 eV.

For electrons, the trap state is supposed to be closer to the CBM because the electrons are localized in the V atom. The positions of the localized state to the CBM are 0.71, 0.9, 1.16, 1.38, 1.68, and 0.3 eV for U_{eff} = 5, 6, 7, 8, 9 and 10 eV. For U_{eff} = 11 eV, no localized state appears in the band gap. So we can find that only U_{eff} = 5 and 10 eV are suitable. But when the U_{eff} value is 5 eV, the density of charges localized on one V atom is

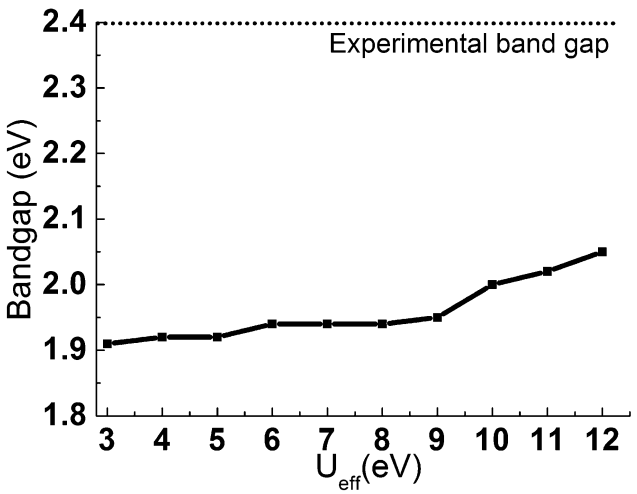

Fig. 1 Band gap *versus* U_{eff}.

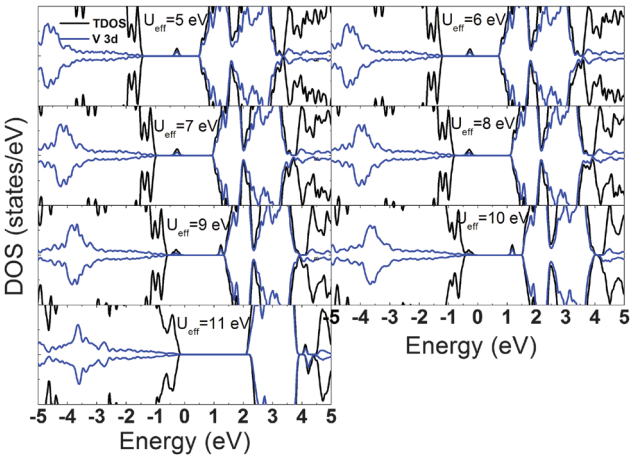

Fig. 2 Total and projected density of states of one extra electron for different U_{eff} values; the Fermi level is set at 0 eV.

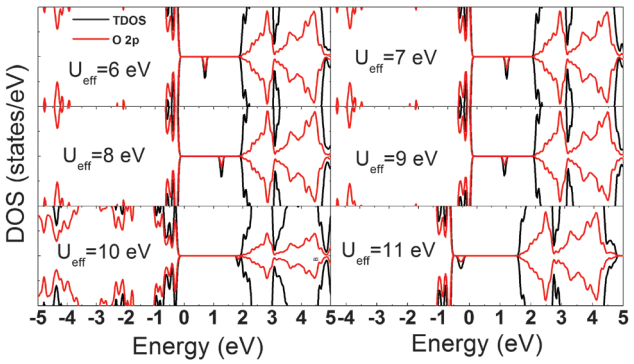

Fig. 3 Total and projected density of states of one extra hole for different U_{eff} values; the Fermi level is set at 0 eV.

only less than 50%. Therefore, we choose the U_{eff} value for electrons to be 10 eV.

For holes, the trap state should be closer to the VBM because the holes are localized in the O atom. The localized state is located above the VBM by 0.80, 1.11, 1.35, and 0.90 eV for U_{eff} = 6, 7, 8, and 9 eV, respectively. For U = 10 eV, the localized state appears in the CB band and for U = 11 eV, the localized states appear in the VB band. So we can find that only U_{eff} = 6 eV and 9 eV are suitable. But when the U_{eff} value is 6 eV, the localized density of charges on one O atom is only less than 40%. Therefore, we choose the U_{eff} value for holes to be 9 eV.

$BiVO_4$ mainly exists in three different crystal phases, tetragonal zircon (tz-), tetragonal scheelite (ts-), and monoclinic scheelite (ms-).[37] Among them, ms-$BiVO_4$ has been found to exhibit the highest photocatalytic activity under visible-light irradiation.[38] tz-$BiVO_4$ has a large band gap of 2.9 eV which is the reason for its lower photocatalytic activity.[38] ms-$BiVO_4$ and ts-$BiVO_4$ have similar band gaps (2.4 eV and 2.3 eV[38]) and lattice parameters (ms-$BiVO_4$: a = 5.195 Å, b = 11.701 Å, c = 5.094 Å; $\alpha = \gamma = 90.00^\circ$, $\beta = 90.38^\circ$;[39] ts-$BiVO_4$: $a = c$ = 5.147 Å; b = 11.722 Å, $\alpha = \gamma = \beta = 90^\circ$),[40] but the monoclinic lattice distortion can induce modifications of the valance-band (VB) electronic structure of ms-$BiVO_4$.[41] In addition, it has been suggested that the increased overlap between

the Bi 6s and the O 2p orbitals would lead to enhanced migration of photogenerated charges in ms-$BiVO_4$.[38]

$BiVO_4$ has been found to exist in the monoclinic scheelite phase at ambient temperature and pressure, and undergoes monoclinic-to-tetragonal phase transition under compression (around 1.5 GPa or 255 °C).[42] The scheelite-type $BiVO_4$ structure consists of isolated VO_4 tetrahedra that are corner connected by BiO_8 dodecahedra. In ts-$BiVO_4$, Bi^{3+} cations are located at the centrosymmetric sites of BiO_8 polyhedra, whereas, the ms-$BiVO_4$ structure exhibits a distorted BiO_8 dodecahedron due to the Bi^{3+} off-centering.

The ball and stick model of monoclinic $BiVO_4$ is shown in Fig. 4a. The experimental lattice parameters are maintained in our calculations. As illustrated in Fig. 4b, it is the polyhedron model of ms-$BiVO_4$ with VO_4 tetrahedra (in gray) and distorted BiO_8 dodecahedra (in purple). In the VO_4 tetrahedra, the lengths of the V–O bond are 1.7849 Å and 1.7829 Å; in the BiO_8 dodecahedra, the lengths of the Bi–O bond are 2.4875 Å, 2.4683 Å, 2.3995 Å, and 2.3991 Å. The different lengths of the Bi–O bonds can reflect the distortion of the BiO_8 dodecahedra, which is consistent with the experimental results.[39]

The orbital-decomposed electron density of states (DOS) is presented in Fig. 5. It reveals that the top of the VB is mainly composed of O 2p states, whereas there is an additional contribution of Bi 6s states. The Bi 6s and O 2p states act as bonding states below the Fermi level, which may make the monoclinic phase $BiVO_4$ energetically more favorable. The CB is principally V 3d states in character with minor contributions from the O 2p states. Cooper and co-workers used a comprehensive approach to understand the electronic structure of monoclinic scheelite bismuth vanadate (ms-$BiVO_4$), including both the valence band (VB) and conduction band (CB) orbital character. They confirmed that the VB maximum and the CB minimum are comprised primarily of O 2p and V 3d orbitals by

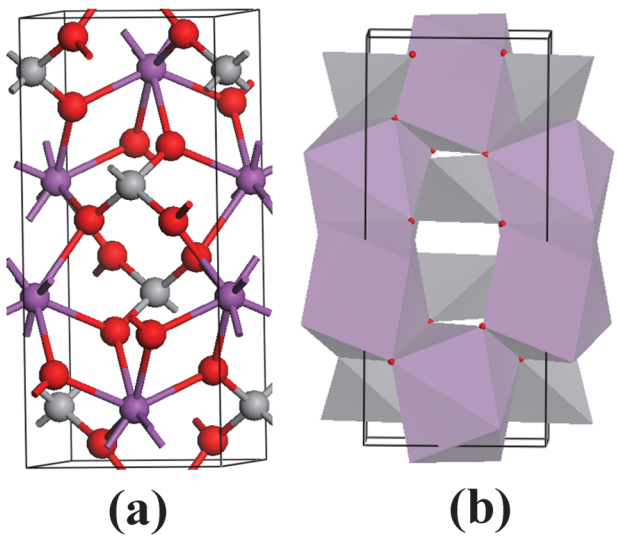

Fig. 4 $BiVO_4$ unit cell: (a) ball and stick model, purple, silver and red balls represent Bi, V and O atoms and (b) polyhedron model with distorted BiO_8 dodecahedra (in purple) and VO_4 tetrahedra (in gray).

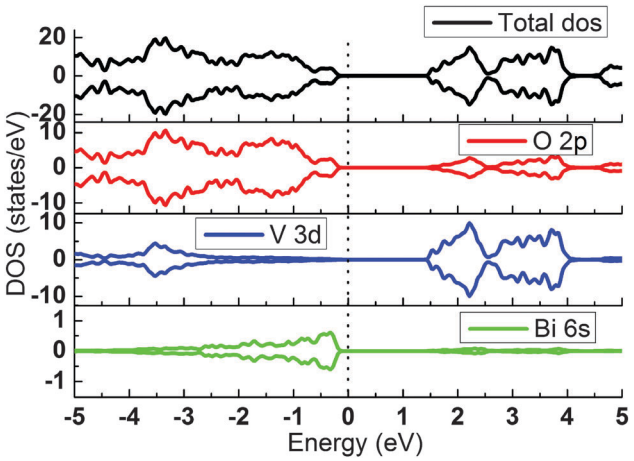

Fig. 5 Total and projected density of states (DOS) of $BiVO_4$; the vertical dashed line indicates the Fermi level.

DFT calculations and experimental data.[35] Our calculated band structure is consistent with their results. In the following small polaron model calculation, we consider that the electron polaron is the V 3d states and the hole polaron is only in the O 2p state.

We considered the addition of an extra electron and hole separately in a supercell of bulk $BiVO_4$ in this study. A compensating uniform background of charges was introduced to re-establish the neutrality of the supercell. For the initial structure, we took the geometry of the neutral $BiVO_4$ ground state, created some small distortions around V or O sites in the periodic cell, and then allowed it to fully relax, keeping the cell size fixed.

As shown in Fig. 6a, adding an electron to $BiVO_4$ creates a localized state within the band gap. After structural relaxation,

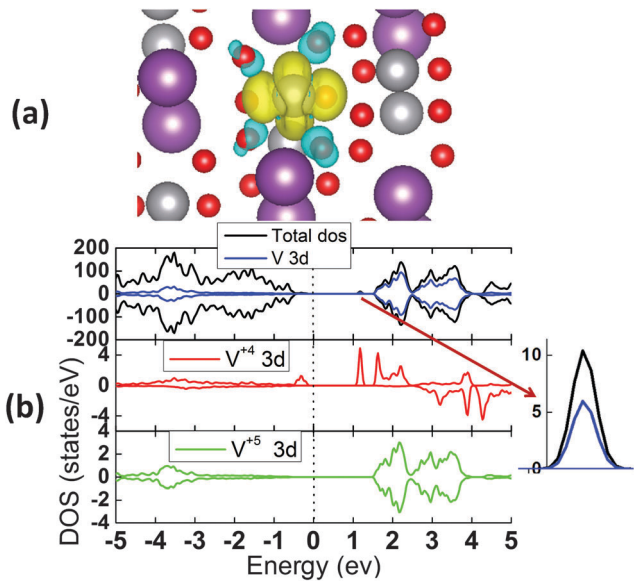

Fig. 6 Spin density contours and total and projected density of states: (a) spin density contours of one extra electron and (b) total and projected density of states of one extra electron; the vertical dashed line indicates the Fermi level.

the excess electron becomes self-trapped at a V^{5+} lattice site, which then becomes formally V^{4+}. Most of the excess charge tends to reside on a V atom, and only a small fraction is on the surrounding four O atoms. The fraction of the localized electron density at the V^{4+} site is approximately 98%. Fig. 6b shows the total and projected density of states of $BiVO_4$ after adding one extra electron. The electron polaron state of the excited electron at the V^{4+} site is V 3d states and it locates 0.30 eV below the CBM. The electron self-trapping is accompanied by significant local distortions around the reduced V^{4+} site, forming a small polaron. Combining Fig. 7a with Table 1, one observes that around the V^{4+} site, the V–O bonds elongate by 0.073 Å and 0.142 Å, respectively. The Bi–O bonds in the second shell region are shortened by approximately 0.100 Å. Distortions seldom occur in other parts of the supercell. Based on the calculations and previous results,[33] we ascribe the increased V–O bond lengths to the partial electron-density filling of the antibonding orbitals formed by the mixing of V 3d and O 2p atomic orbitals. A possible reason for the decreased Bi–O bond lengths is that stronger hybridization between Bi 6s and O 2p states and unoccupied Bi 6p states reduces the antibonding interaction.

Because the VBM of $BiVO_4$ shows O 2p dominant character with a non-negligible contribution of Bi 6s states,[33,34] it is more difficult to localize a hole than an electron. The spin density contours in Fig. 8a clearly demonstrates the hole localized on the selected O atom. About 70% of the charge density of the hole is predicted to reside on the O site, and the rest of the charge spreads on the surrounding O atoms. After the hole localized, the O^{2-} becomes formally O^{-} and the hole state turns out to lie about 0.9 eV above the top of the VB as shown in Fig. 8b. The hole self-trapping is accompanied by local lattice distortions to yield a highly distorted BiO_8 polyhedron, indicating the formation of small polarons. The polaronic distortion involving all of the V–O and Bi–O bonds close to the hole is shown in Fig. 7b and Table 2. The V–O bond elongates by 0.080 Å and the Bi–O bonds elongate by 0.204 Å and 0.144 Å. In the second shell region, the changes in Bi–O bond lengths vary between −0.163 Å and 0.151 Å, and the V–O bond lengths are shortened by approximately 0.081 Å. The bond length changes

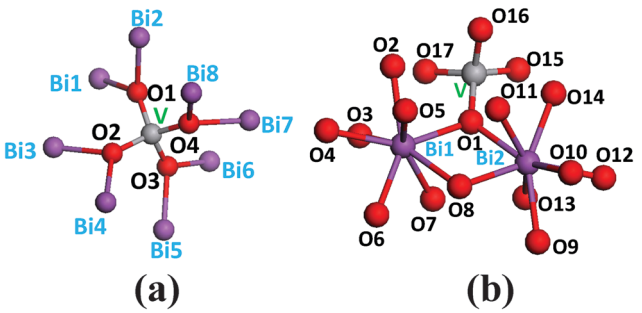

Fig. 7 Geometry with an extra (a) electron and (b) hole; the electron is localized on the V site in (a) and the hole is localized on the O1 site in (b).

Table 1 Geometry with an excess electron before and after relaxation. The structure is shown in Fig. 7a

Structure with electrons	Before relaxation (Å)	After relaxation (Å)	Change (Å)
V–O1	1.785	1.858	+0.073
V–O2	1.785	1.858	+0.073
V–O3	1.783	1.925	+0.142
V–O4	1.783	1.925	+0.142
Bi1–O1	2.399	2.278	−0.121
Bi2–O1	2.468	2.323	−0.145
Bi3–O2	2.487	2.366	−0.121
Bi4–O2	2.399	2.253	−0.146
Bi5–O3	2.487	2.366	−0.121
Bi6–O3	2.399	2.253	−0.146
Bi7–O4	2.468	2.323	−0.145
Bi8–O4	2.399	2.278	−0.121

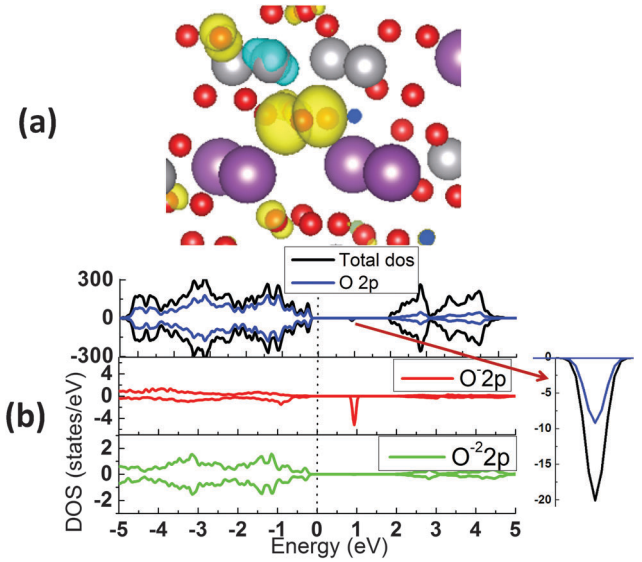

Fig. 8 Spin density contours and total and projected density of states: (a) spin density contours of one extra hole, and (b) total and projected density of states of one extra hole; the vertical dashed line indicates the Fermi level.

Table 2 Geometry with an excess hole before and after relaxation. The structure is shown in Fig. 7b

Structure with holes	Before relaxation (Å)	After relaxation (Å)	Change (Å)
Bi1–O1	2.487	2.631	+0.144
Bi2–O1	2.399	2.603	+0.204
V–O1	1.785	1.865	+0.08
Bi1–O2	2.487	2.599	+0.112
Bi1–O3	2.399	2.346	−0.053
Bi1–O4	2.399	2.513	+0.114
Bi1–O5	2.468	2.345	−0.123
Bi1–O6	2.468	2.371	−0.097
Bi1–O7	2.399	2.401	+0.002
Bi1–O8	2.399	2.530	+0.131
Bi2–O8	2.487	2.638	+0.151
Bi2–O9	2.399	2.366	−0.033
Bi2–O10	2.468	2.305	−0.163
Bi2–O11	2.399	2.360	−0.039
Bi2–O12	2.468	2.464	−0.004
Bi2–O13	2.399	2.427	+0.028
Bi2–O14	2.487	2.597	+0.11
V–O15	1.785	1.719	−0.066
V–O16	1.783	1.705	−0.078
V–O17	1.783	1.684	−0.099

very little beyond the second shell region. After adding a hole (namely removing an electron from) at an O site, the V–O and Bi–O bonding orbitals will become weakened and as a result the V–O bonds and Bi–O bonds become longer.

A small polaron may undergo thermally activated hopping from site to site.[43] The activation energy for polaron hopping can be estimated by calculating the variation of potential energy as the polaronic lattice configuration is displaced from the initial to the final geometry; if the initial and the final states are identical, the transition state may occur midway between the two local minima. Using a 192-atom $2 \times 2 \times 2$ supercell, we computed activation energies employing the methodology described in the previous section. To identify saddle-point geometries for polaron hopping, we generated configurations with atomic positions at the midpoint between those corresponding to the initial and final polaron sites along a particular crystal orientation. The calculated activation energies of electron/hole transfer, denoted as $\Delta G_e/\Delta G_h$, for all the low-index crystal orientations are listed in Table 3. The energy barriers for electron transfer are in the range from 0.194 to 0.576 eV for different directions, which reflect the anisotropy properties of the $BiVO_4$ crystal. In ref. 26, the authors demonstrated that the electron transport in $BiVO_4$ is described by a thermally activated small polaron hopping mechanism from 250 to 400 K. When the electron transport takes place between V^{4+} and V^{5+}, they got the activation energy of about 0.29 eV. In our calculation, the activation energy of [100] is about 0.3 eV, which is consistent with the experimental values. So, the methods we used are appropriate for dealing with charge transport in $BiVO_4$.

The energy barriers for hole transfer are in the range from 0.433 to 0.848 eV. There are no direction experimental activation values of $BiVO_4$ for comparison. In the case of TiO_2, the activation energy for hole transfer is about 0.6 eV.[20] Our calculated values have the same magnitude as that in TiO_2. In addition, the activation energy for hole transport is larger than the activation energy of electron transfer, which is consistent with the experimental result that the electron is transferred faster than the hole.

We assumed that electron/hole transport in $BiVO_4$ follows an adiabatic small polaron hopping mechanism.[26] The processes of electron and hole migration can be described by gradual changes in the distorted lattice configurations between two adjacent polaron configurations along the selected crystal orientation. Based on Einstein's formula, the electron and hole mobilities were calculated. As shown in Table 3, the mobilities of electrons are much larger than those of holes in the same crystal orientations, and the mobility of an electron is the largest along the [010] direction, and the mobility of a hole is the largest along the [100] direction. The mobility of an electron along [010] is the largest one which has a value of 8.53×10^{-4} $cm^2\ V^{-1}\ s^{-1}$. The mobility of a hole along [100] is the largest one which has a value of 5.64×10^{-8} $cm^2\ V^{-1}\ s^{-1}$. We realized that the value of our calculated mobility is much smaller than the values reported so far for this material system. There are several reasons for this difference. Firstly, it has intrinsic poor carrier transport properties in $BiVO_4$. Time-resolved microwave conductivity (TRMC) measurements reveal a carrier mobility of $\sim 4 \times 10^{-2}$ $cm^2\ V^{-1}\ s^{-1}$ for undoped $BiVO_4$ under ~ 1 Sun illumination conditions, which is at least 1–2 orders of magnitude lower than that in a typical semiconductor for water splitting.[44] Secondly, despite the low mobility, high quantum efficiencies can nevertheless be achieved in $BiVO_4$ due to the long lifetime of the photogenerated charge carriers (~ 40 ns), which leads to relatively long carrier diffusion lengths (~ 70 nm). The long lifetime implies that there are few intrinsic recombination centers, which indicated that $BiVO_4$ is a highly "defect-tolerant" material.[44] Thirdly, doping can improve the photocurrent and increase the quantum efficiencies remarkably. Berglund *et al.* synthesized films with a $Bi:V:M_o:W$ atomic ratio of 46 : 46 : 6 : 2 (6% M_o, 2% W), which demonstrates the best PEC performance with photocurrent densities 10 times higher than that for pure $BiVO_4$ and is greater than that previously reported for M_o and W containing $BiVO_4$. They also demonstrated that backside illumination utilizes light scattering off the irregular surface structure resulting in 30–45% higher photocurrent densities than frontside illumination.[45] This may be explained by the long lifetime photogenerated charge carriers, the long carrier diffusion lengths and the increased charge density caused by doping.

We must emphasize that what we calculated are intrinsic diffusional mobilities for $BiVO_4$ along different low-index crystal orientations. In contrast, experimentally measured mobility is typically drift or Hall mobility.[26] Thus, the calculated quantities are not directly comparable to experimental values, a more complete model would have to include other factors, such as structural defects and disorder, applied voltage, and so on. But a comparison of the relative order of mobilities along different directions is reasonable. With the correct carrier conductor mechanism, the main goal of our work is the comparison of the relative order of the mobility along different crystal directions.

To estimate which are the highly exposed facets, slabs with six stoichiometric repeated layers were constructed for each low-index surface. The computed total energies of the slabs, together with their corresponding numbers of $BiVO_4$ units, were then fitted into the following equation used to calculate the surface formation energy γ, $\gamma = (E_{slab} - nE_{BiVO_4})/2A$, where E_{slab} and E_{BiVO_4} are the total energy of the slab and bulk, n is the number of $BiVO_4$ units in the slab, and $2A$ is the total exposed area of the two identical sides of the slab. The computed

Table 3 Electron and hole transfer paths and the corresponding facets. ΔG_e and ΔG_h are the activation energy of electrons and holes, μ_e and μ_h are the mobility of electrons and holes, and γ is the surface energy

Crystal axis	Crystal surface	ΔG_e (eV)	ΔG_h (eV)	μ_e ($cm^2\ V^{-1}\ s^{-1}$)	μ_h ($cm^2\ V^{-1}\ s^{-1}$)	γ ($J\ m^{-2}$)
[010]	(010)	0.226	0.848	8.53×10^{-4}	3.10×10^{-14}	0.20
[110]	(110)	0.576	0.707	1.36×10^{-9}	8.63×10^{-12}	0.21
[100]	(100)	0.301	0.433	9.26×10^{-6}	5.64×10^{-8}	0.50
[001]	(001)	0.194	0.734	5.56×10^{-4}	4.81×10^{-13}	0.48
[101]	(101)	0.345	0.799	3.29×10^{-6}	7.90×10^{-14}	0.42
[011]	(011)	0.231	0.844	8.36×10^{-4}	4.30×10^{-14}	0.20
[111]	(111)	0.549	0.831	1.12×10^{-9}	2.07×10^{-14}	0.35

surface energies are shown in Table 3. The smaller the surface energy, the more stable the corresponding facet. Based on the calculated results, the relative stability trend of low-index surfaces is predicted to be (010) = (011) ≈ (110) > (111) > (001) > (100). Our results are in good agreement with the observed morphology of $BiVO_4$, in which (010) and (110) are highly exposed.[9]

We are able to obtain the following results from our calculations. Firstly, the mobility of an electron is much larger than that of a hole in the same crystal orientations. Secondly, the facets of (010) and (110) of $BiVO_4$ are highly exposed. Finally, in the highly exposed facets, the mobility of an electron is the largest along the [010] direction, and the mobility of a hole is the largest along the [110] direction.

Our recent experiments on $BiVO_4$ found that photo-deposition of metals/metal oxides has facet-selective properties.[9] The photo-depositions of metals on the surface of $BiVO_4$ were carried out using $HAuCl_4$ (H_2PtCl_6 and $AgNO_3$) as a precursor and water as a hole scavenger. SEM images clearly show that the particles of Ag, Au, and Pt are solely deposited on the (010) facets. Namely, the photogenerated electrons are readily available for the reduction reaction on the (010) facets. Photo-oxidation depositions of Mn^{2+} or Pb^{2+} ions on $BiVO_4$ were performed with IO_3^- as an electron acceptor. The formation of PbO_2 and MnO_x oxides is an indication that the photo-oxidation selectively takes place on the (110) facets, that is, the photogenerated holes tend to migrate to the (110) facets for selective metal oxidation. The photo-deposition of dual precursors with simultaneous reduction and oxidation was also investigated. It is interesting to note that the Au, Pt, and Ag particles are still selectively photo-deposited on the (010) facets, while the MnO_x and PbO_2 particles are loaded only on the (110) facets of $BiVO_4$. All of these results unambiguously reveal that the photogenerated electrons and holes tend to accumulate on the (010) and (110) facets, respectively, which results in the reduction and oxidation reactions taking place on the corresponding (010) and (110) facets.

In the process of photocatalytic reactions, some of the photogenerated electrons and holes migrate to the surface of the semiconductor and then participate in reduction and oxidation reactions. The semiconductor can be divided into a bulk region and a surface region. Here, we only investigated the transfer of photogenerated electrons/holes in the bulk region. This means that the conditions of the surface, such as surface band bending and surface energetic difference, are neglected in this work.

According to the calculated results and our previous experimental results, we can see that there is a parallel relationship between the carrier's mobility along the crystal axis and the carrier's preferred accumulation on the corresponding crystal facets. The mobility of electrons (or holes) along the crystal axis [*hkl*] might be essentially related to the charge separation among the corresponding facets (*hkl*). So it could be proposed that, as shown in Fig. 9, for the exposed facets of a crystal, the mobility of electrons (or holes) along the crystal axis [*hkl*] is the largest among all possible crystal axes, and the photogenerated electrons (or holes) tend to be accumulated on the corresponding facet (*hkl*), when the surface factors like surface band bending, surface energetic differences, *etc*. are not considered.

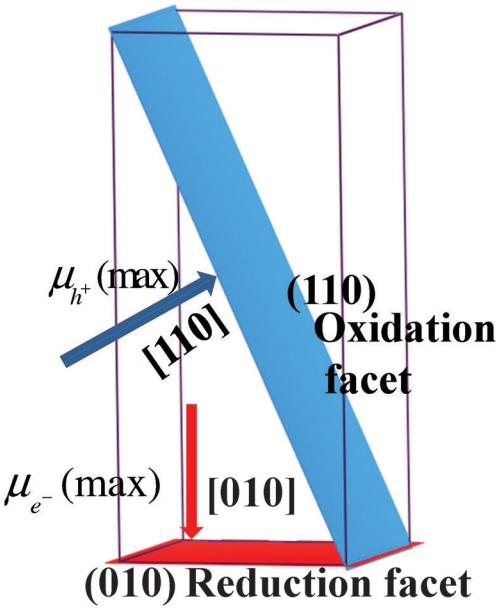

Fig. 9 Electron (or hole) transfer paths along the crystal axis [*hkl*] and the corresponding facet (*hkl*).

4. Conclusions

In summary, we have studied the charge migration in $BiVO_4$ employing the formalism of DFT with Hubbard *U* corrections and Marcus/Holstein theory using a small polaron model. We calculated the activation energy and the mobility of carriers in seven low-index crystal orientations. The surface energies of these seven low-index surfaces were also calculated. The results show that (1) the mobility of electrons is much larger than that of holes along the same crystal axis orientations, (2) the facets of (010) and (110) are highly exposed, and (3) for the exposed facets of (010) and (110), the mobility of electrons along [010] is five orders of magnitude larger than that of the [110] direction and the mobility of holes along [110] is two orders of magnitude larger than that of the [010] direction. Our calculated mobilities and the experimental results reveal that there is a parallel relationship between the carrier mobility along the crystal axis and the carrier preferred accumulation on the corresponding crystal facets. The mobility of electrons (or holes) along the crystal axis [*hkl*] might be essentially related to the charge separation among the corresponding facets (*hkl*). Namely, for exposed facets of the crystal, it could be proposed that the mobility of electrons (or holes) along the crystal axis [*hkl*] is the largest among all possible crystal axes, and the photogenerated electrons (or holes) tend to accumulate on the corresponding facet (*hkl*), when the surface factors like surface band bending, surface energetic differences, *etc*. are not considered. Our theoretical understanding of spatial charge separation between different crystal facets of $BiVO_4$ may give a greater understanding of charge separation in semiconductor based photocatalysts.

Acknowledgements

We would like to acknowledge the support of the National Natural Science Foundation of China under Grants 21473183 and 21361140346.

References

1 K. Maeda, K. Teramura, D. L. Lu, T. Takata, N. Saito, Y. Inoue and K. Domen, *Nature*, 2006, **440**, 295.
2 H. G. Kim, D. W. Hwang and J. S. Lee, *J. Am. Chem. Soc.*, 2004, **126**, 8912–8913.
3 X. B. Chen, L. Liu, P. Y. Yu and S. S. Mao, *Science*, 2011, **331**, 746–750.
4 A. Kudo and Y. Miseki, *Chem. Soc. Rev.*, 2009, **38**, 253–278.
5 F. E. Osterloh, *Chem. Mater.*, 2008, **20**, 35–54.
6 K. Maeda, A. Xiong, T. Yoshinaga, T. Ikeda, N. Sakamoto, T. Hisatomi, M. Takashima, D. Lu, M. Kanehara, T. Setoyama, T. Teranishi and K. Domen, *Angew. Chem., Int. Ed.*, 2010, **49**, 4096–4099.
7 X. Zong, H. J. Yan, G. P. Wu, G. J. Ma, F. Y. Wen, L. Wang and C. Li, *J. Am. Chem. Soc.*, 2008, **130**, 7176–7177.
8 X. Wang, Q. Xu, M. Li, S. Shen, X. Wang, Y. Wang, Z. Feng, J. Shi, H. Han and C. Li, *Angew. Chem., Int. Ed.*, 2012, **51**, 13089–13092.
9 R. Li, F. Zhang, D. Wang, J. Yang, M. Li, J. Zhu, X. Zhou, H. Han and C. Li, *Nat. Commun.*, 2013, **4**, 1432–1438.
10 X. Wang, R. Li, Q. Xu, H. Han and C. Li, *Acta Phys.-Chim. Sin.*, 2013, **29**, 1566–1571.
11 L. Zhang, W. Wang, S. Sun, D. Jiang and E. Gao, *Appl. Catal., B*, 2015, **162**, 470–474.
12 T. Ohno, K. Sarukawa and M. Matsumura, *New J. Chem.*, 2002, **26**, 1167–1170.
13 Y. Miseki, H. Kato and A. Kudo, *Energy Environ. Sci.*, 2009, **2**, 306–314.
14 R. A. Marcus, *Rev. Mod. Phys.*, 1993, **65**, 599–610.
15 T. Holstein, *Ann. Phys.*, 2000, **281**, 725–773.
16 D. Matthey, J. G. Wang, S. Wendt, J. Matthiesen, R. Schaub, E. Laegsgaard, B. Hammer and F. Besenbacher, *Science*, 2007, **315**, 1692–1696.
17 H. G. Yang, C. H. Sun, S. Z. Qiao, J. Zou, G. Liu, S. C. Smith, H. M. Cheng and G. Q. Lu, *Nature*, 2008, **453**, 638–641.
18 M. Setvin, U. Aschauer, P. Scheiber, Y.-F. Li, W. Hou, M. Schmid, A. Selloni and U. Diebold, *Science*, 2013, **341**, 988–991.
19 N. A. Deskins and M. Dupuis, *Phys. Rev. B: Condens. Matter Mater. Phys.*, 2007, **75**, 195212.
20 N. A. Deskins and M. Dupuis, *J. Phys. Chem. C*, 2009, **113**, 346–358.
21 E. Yagi, R. R. Hasiguri and M. Aono, *Phys. Rev. B: Condens. Matter Mater. Phys.*, 1996, **54**, 7945–7956.
22 P. K. Schelling and J. W. Halley, *Phys. Rev. B: Condens. Matter Mater. Phys.*, 2000, **62**, 3241–3245.
23 S. R. Elliott, *The Physics and Chemistry of Solids*, Wiley, West Sussex, 1998.
24 P. A. Cox, *The Electronic Structure and Chemistry of Solids*, Oxford University Press, New York, 1987.
25 A. J. E. Rettie, W. D. Chemelewski, J. Lindemuth, J. S. McCloy, L. G. Marshall, J. S. Zhou, D. Emin and C. B. Mullins, *Appl. Phys. Lett.*, 2015, **106**, 022106.
26 A. J. E. Rettie, H. C. Lee, L. G. Marshall, J.-F. Lin, C. Capan, J. Lindemuth, J. S. McCloy, J. Zhou, A. J. Bard and C. B. Mullins, *J. Am. Chem. Soc.*, 2013, **135**, 11389–11396.
27 G. Kresse and J. Furthmüller, *Phys. Rev. B: Condens. Matter Mater. Phys.*, 1996, **54**, 11169–11186.
28 G. Kresse and J. Furthmüller, *Comput. Mater. Sci.*, 1996, **6**, 15–50.
29 J. P. Perdew, K. Burke and M. Ernzerhof, *Phys. Rev. Lett.*, 1996, **77**, 3865–3868.
30 P. E. Blochl, *Phys. Rev. B: Condens. Matter Mater. Phys.*, 1994, **50**, 17953–17979.
31 G. Kresse and J. Joubert, *Phys. Rev. B: Condens. Matter Mater. Phys.*, 1999, **59**, 1758–1775.
32 S. L. Dudarev, G. A. Botton, S. Y. Savrasov, C. J. Humphreys and A. P. Sutton, *Phys. Rev. B: Condens. Matter Mater. Phys.*, 1997, **57**, 1505–1509.
33 M. Oshikiri, M. Boero, J. Ye, Z. Zou and G. Kido, *J. Chem. Phys.*, 2002, **117**, 7313–7318.
34 J. Yang, D. Wang, X. Zhou and C. Li, *Chem. – Eur. J.*, 2013, **19**, 1320–1326.
35 J. K. Cooper, S. Gul, F. M. Toma, L. Chen, P.-A. Glans, J. Guo, J. W. Ager, J. Yano and I. D. Sharp, *Chem. Mater.*, 2014, **26**, 5365–5373.
36 R. L. Frost, D. A. Henry, M. L. Weier and M. W. Martens, *J. Raman Spectrosc.*, 2006, **37**, 722–732.
37 D. Bierlein and A. W. Sleight, *Solid State Commun.*, 1975, **16**, 69–70.
38 S. Tokunaga, H. Kato and A. Kudo, *Chem. Mater.*, 2001, **13**, 4624–4628.
39 A. W. Sleight, H.-Y. Chen, A. Ferretti and D. E. Cox, *Mater. Res. Bull.*, 1979, **14**, 1571–1581.
40 L. Jian-Cheng, C. Jia-Ping and L. de-Yu, *Acta Phys. Sin.*, 1983, **32**, 1053–1060.
41 A. Walsh, Y. Yan, M. H. Huda, M. M. Al-Jassim and S. H. Wei, *Chem. Mater.*, 2009, **21**, 547–551.
42 R. M. Hazen and J. W. E. Mariathasan, *Science*, 1982, **216**, 991–993.
43 A. J. Bosman and H. J. van Daal, *Adv. Phys.*, 1970, **19**, 1–117.
44 F. F. Abdi, T. J. Savenije, M. M. May, B. Dam and R. van de Krol, *J. Phys. Chem. Lett.*, 2013, **4**, 2752–2757.
45 S. P. Berglund, A. J. E. Rettie, S. Hoang and C. B. Mullins, *Phys. Chem. Chem. Phys.*, 2012, **14**, 7065–7075.

